Coherent Imaging with X-ray Free-Electron Lasers

H. N. Chapman

This document has been published in

Manuel Angst, Thomas Brückel, Dieter Richter, Reiner Zorn (Eds.):
Scattering Methods for Condensed Matter Research: Towards Novel Applications at Future Sources
Lecture Notes of the 43rd IFF Spring School 2012
Schriften des Forschungszentrums Jülich / Reihe Schlüsseltechnologien / Key Technologies, Vol. 33
JCNS, PGI, ICS, IAS
Forschungszentrum Jülich GmbH, JCNS, PGI, ICS, IAS, 2012
ISBN: 978-3-89336-759-7

D 10 Coherent Imaging with X-ray Free-Electron Lasers[1]

H. N. Chapman
Center for Free-Electron Laser Science
DESY, Hamburg

Contents

[1]Lecture Notes of the 43rd IFF Spring School "Scattering Methods for Condensed Matter Research: Towards Novel Applications at Future Sources" (Forschungszentrum Jülich, 2012).

1 Introduction

X-ray free-electron lasers (FELs) such as the Linac Coherent Light Source (LCLS) [1] produce laser-like pulses of X-rays of 10 fs to 300 fs duration and up to about 10^{13} photons per pulse. Just as with the introduction of the synchrotron, X-ray FELs promise to have a great impact on many scientific disciplines by opening up the study of materials at the length scale of interatomic distances and at the corresponding time scales of atomic motion. In condensed matter science, for example, materials properties can be drastically altered by inducing transient structures using ultrafast light pulses [2]. Similarly, matter at extreme limits of temperature and pressure, similar to conditions in the cores of stars and planets, can be created transiently in the laboratory using intense optical pulses. The extremely intense and brief pulses delivered by X-ray FELs opens up the direct imaging of processes in these systems, which previously could only be studied by spectroscopic means. In the biological sciences, time-resolved X-ray crystallography has elucidated the atomic motions that occur on stimulation of light-sensitive proteins [3]. This field will experience a dramatic increase of capability with FEL sources. The extreme irradiance[2] of the pulses will let us shrink crystal sizes all the way down to single molecules, giving three-dimensional movies of conformational dynamics and chemical reactions, and allowing the imaging of macromolecules that cannot be easily crystallized.

X-ray crystallography is indeed the inspiration for the methods of imaging at X-ray FELs [4]. Crystallography can obtain atomic-resolution images of protein macromolecules without the use of a lens, based on the interpretation of the coherent scattering pattern detected in the far field. Since this method is lensless, there are no technological limitations to the achievable resolution caused by the perfection of objective lenses that can be made. Instead, the image is synthesized from the measured diffraction intensities. Each intensity sample is related to the strength of each spatial frequency component of the synthesized image. The shift of each spatial frequency component in real space is given by the corresponding phase of the diffracted wavefield. Crucially, this information cannot be obtained by measurement. The correct image, formed by the sum of the correctly positioned periodic components, cannot be synthesized without this information. This so-called phase problem has been largely solved in protein crystallography by constraining the phases through additional information about the structure such its atomicity (if scattering to high enough resolution was obtained), protein sequence, or known similar structure. Anomalous diffraction methods can be used to determine the locations of heavy atoms, which in turn can act as holographic references to obtain the remaining image. This general imaging strategy works even better for non-crystalline materials, since the information content of a continuous diffraction pattern of a non-periodic object is large enough to completely constrain the phases, allowing *ab initio* reconstruction of both two- and three-dimensional images [5, 6]. The phase retrieval algorithms in this case were first developed in the context of electron microscopy [7] and optical remote sensing [8].

The generalization of crystallography tol non-periodic objects requires sufficient spatial and temporal coherence of the illumination wavefield so that the scattered waves from extreme points in the object interfere to create the fringe pattern on the detector that encodes their separation. The lack of crystallinity does come at a severe cost of diffraction signal, since the integrated Bragg intensity is proportional to the number of units in the crystal [9] and the number of repeats in even small protein crystals can number in the billions. Unfortunately the lower

[2]Pulse irradiance is given in units of photons per unit area and time. It is often referred to as "intensity", although in crystallography that word commonly means "diffracted counts" which is the meaning employed in this chapter.

signal cannot simply be compensated by longer exposure, since biological materials can only withstand a limited dose before they are destroyed by the very beam that is used to obtain the image [10]. But here the ultrafast pulses of X-ray FELs come to the rescue, by diffracting from the sample before the effects of radiation damage have set in [11]. There is strong evidence that this concept of "diffraction before destruction" holds to atomic resolution, at doses over 100 times higher than can be tolerated by slow exposures [12]. The development of this imaging technique is following two tracks: application to unique structures, such as cells or soot particles, that can only be imaged in a single shot; and to reproducible objects, such as viruses, macromolecular complexes, and protein nanocrystals, and where signals can be accumulated over many copies in a rapid series of diffraction measurements. These are extremely active fields of research, and progress is fast despite the fact that only a single hard X-ray FEL facility currently exists.

In this lecture, a brief description of coherent scattering and iterative phasing techniques are described, showing how 2D and 3D images of finite-size non-periodic objects can be recovered from diffraction data. Examples of the application of this technique are presented from experiments carried out at the FLASH soft X-ray FEL in Hamburg and the LCLS, and the research of single-particle diffractive imaging and "diffraction before destruction" is summarized, including computational and experimental investigations of the rate of perturbation of a structure under intense X-ray illumination.

2 Coherent Scattering from Isolated Objects

The interaction of x-rays with matter can be described by the inhomogeneous Helmholtz equation,

$$(\nabla^2 + k^2)\psi(\mathbf{x}) = \Phi(\mathbf{x})\psi(\mathbf{x}) \tag{1}$$

for an incident plane wave of wavelength λ or wavenumber $k = 2\pi/\lambda$. The scattering potential of a static and non-magnetic object may be expressed as

$$\Phi(\mathbf{x}) = k^2(1 - n^2(\mathbf{x})) = 4\pi r_e \rho(\mathbf{x}) \tag{2}$$

where n is the refractive index, r_e the classical radius of the electron, and $\rho(\mathbf{x})$ the electron density of the object. In the Born approximation the solution to (1) is of the form

$$\psi(\mathbf{x}) = e^{i\mathbf{k}_{\rm in}\cdot\mathbf{x}} + \frac{e^{ikr}}{r} f(\mathbf{q}) \tag{3}$$

where

$$f(\mathbf{q}) = -r_e \int \rho(\mathbf{x}) \exp(i\mathbf{q}\cdot\mathbf{x})\, d\mathbf{x}. \tag{4}$$

and $\mathbf{q} = \mathbf{k}_{\rm out} - \mathbf{k}_{\rm in}$ is the photon momentum transfer. The physical picture that explains the form of the scattering factor $f(\mathbf{q})$ is shown in Fig. 1 (a). A ray scattered in a direction $\mathbf{k}_{\rm out}$ from a point $\mathbf{x}_1$ will acquire a path difference of $\ell_1 = (\mathbf{x}_1 \cdot \hat{\mathbf{k}}_{\rm out} - \mathbf{x}_1 \cdot \hat{\mathbf{k}}_{\rm in})$ relative to a ray scattering from the origin $\mathbf{O}$, where $\hat{\mathbf{k}}$ are unit vectors. This is the difference of the lengths of the thick lines in Fig. 1 (a). The accumulated phase will therefore be $\phi_1 = (2\pi/\lambda)\ell_1 = \mathbf{x}_1 \cdot \mathbf{q}$. The point scatterer itself may cause a modification to the wave by the complex constant f_1, giving a scattering $f_1 \exp(i\phi_1) = f_1 \exp(i\mathbf{x}_1 \cdot \mathbf{q})$. Equation (4) is simply the integration over all scatterers in the object. The object's electron density is assumed to be continuous, although it can certainly be atomistic and may possess translational periodicity (i.e. be a crystal).

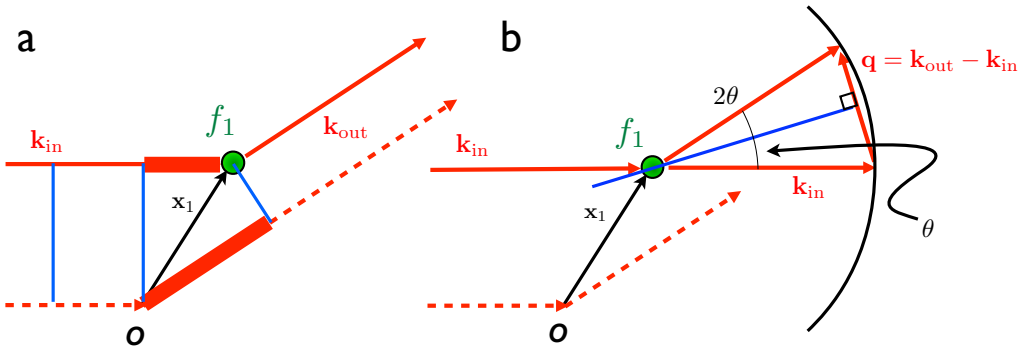

Fig. 1: *The far-field scattering geometry and the Ewald-sphere construction.*

Equation (4) states that the scattering amplitude f is given by the Fourier transform of the electron density. That is, the strength of diffraction in the direction $\mathbf{k}_{\rm out}$ only depends on the Fourier component $\tilde{\rho}(\mathbf{q})$, where we define the Fourier transform as

$$\tilde{g}(\mathbf{q}) \equiv \mathcal{F}\{g(\mathbf{x})\} \equiv \int g(\mathbf{x}) \exp(i\mathbf{x}\cdot\mathbf{q})\, d\mathbf{x}. \tag{5}$$

This component is a particular spatial frequency in the object, which may be thought of as a volume grating of a particular wavenumber $|\mathbf{q}|$ and direction $\hat{\mathbf{q}}$. From Fig. 1 (b), it is seen that the magnitude of $\mathbf{q}$ is given simply by

$$|\mathbf{q}| = 2|\mathbf{k}| \sin\theta = \frac{4\pi}{\lambda} \sin\theta \tag{6}$$

for a scattering angle 2θ, and that due to the conservation of $\mathbf{k}$ (that is, elastic scattering) the vector $\mathbf{q}$ lies on the surface of a sphere (called the Ewald sphere). We see from the diagram in Fig. 1 (b) that the scattered ray appears to reflect at an angle θ from a plane normal to $\mathbf{q}$. That is, the ray reflects from the volume grating which is tilted at the angle θ relative to the incoming wave-vector. The ray only reflects if the period of the volume grating, $d = 2\pi/|\mathbf{q}|$ satisfies Eqn. (6), which is to say $d = \lambda/(2\sin\theta)$ which is well recognized as Bragg's law. We stress that although Bragg's law and the Ewald sphere construction are well known concepts in crystallography, there is no requirement of periodicity of the object in the derivation or application of these concepts.

A typical coherent diffraction experiment illuminates a sample of electron density $\rho(\mathbf{x})$ (or refractive index $n(\mathbf{x})$) with a quasi-monochromatic plane wave and measures the diffraction pattern in the far field with a planar detector (such as a bare CCD). This is a measure of the intensity of the wavefield, given by

$$I(\mathbf{q}) = I_0\, \Omega_p\, P\, r_e^2\, |\tilde{\rho}(\mathbf{q})|^2\,, \tag{7}$$

for pixels of solid angle Ω_p, and where P is the polarization factor. The mapping from pixel coordinate to $\mathbf{q}$ is easily obtained by the geometry shown in Fig. 1 where $\mathbf{k}_{\rm out}$ points in the direction of the pixel. Note that in a single exposure in this geometry records only information about the object for spatial frequencies that lie on the Ewald sphere. Other frequencies are missing in the measurement and the only way to record the full 3D information is to record

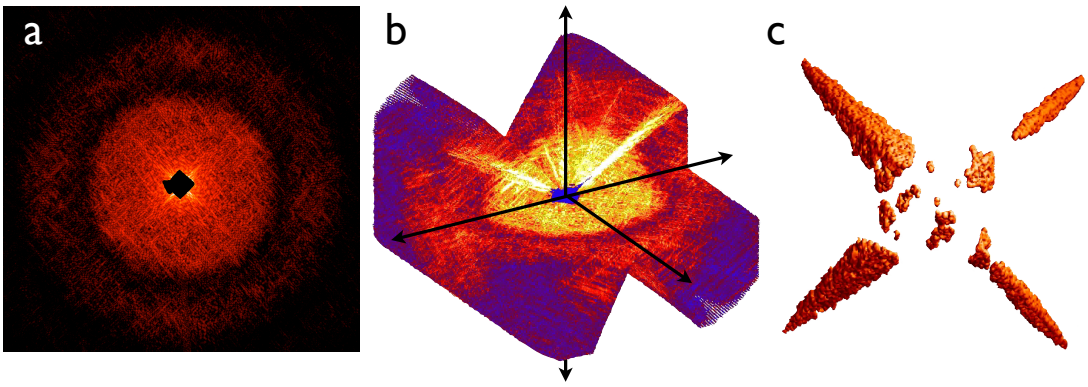

Fig. 2: *Diffraction data collected from a 3D test object, showing (a) a diffraction pattern recorded at a single orientation, (b) 3D diffraction intensities collected at orientations from* $-70°$ *to* $+70°$*, and (c) the reconstructed volume image [6].*

additional diffraction patterns for different orientations of the object relative to the incident beam. Rotating the sample rotates its Fourier spectrum such that it sweeps across the Ewald sphere. From the point of view of the object, the measurements at different orientations can be thought of as orienting the Ewald sphere at different rotations (about the point $\mathbf{q} = 0$) so that it samples the 3D intensities $|\tilde{\rho}(\mathbf{q})|^2$. An example of 3D diffraction data collected at a synchrotron beamline is shown in Fig. 2.

Since the sample is completely destroyed by the interaction with a single high-irradiance FEL pulse, one object can only give rise to a single measurement (or possibly multiple simultaneous measurements). Full 3D information therefore requires combining many diffraction patterns, each from a different orientation of an identical copy of the object. Combining data from many patterns is also needed to increase the overall signal. A calculated single molecule diffraction pattern is shown in Fig. 3 for an incident pulse fluence of 10^{12} photons focused to a 0.3-μm diameter spot at 8 keV photon energy ($10^6\,\mathrm{J/cm^2}$), corresponding to an irradiance of $3 \times 10^{19}\,\mathrm{W/cm^2}$ with a pulse duration of 30 fs. The pattern is noisy because of low photon counts (most detector pixel values are zero or one photon count). Therefore, even with the extremely high irradiances from an X-ray FEL, some averaging of the signal from many particles is required to increase the signal to noise ratio even at a single orientation. The photon count per pixel of solid-angle Ω_p per shot, averaged over shells of q, for biological material can be estimated by

$$\langle I(q)\rangle_q = I_0\,\Omega_p\,P\,r_e^2\,\left\langle|\tilde{\rho}(q)|^2\right\rangle_q = I_0\,\Omega_p\,P\,r_e^2\,N_{\mathrm{atom}}\,|f|^2, \tag{8}$$

where N_{atom} are the number of atoms in the molecule, and f is an average atomic scattering factor (e.g. close to that of carbon). Full diffraction information requires sampling at the Shannon rate Δq_S as described in Sec. 3.1 on p. 10.9. In this case we have $\Omega_p \approx (\lambda/4\pi)^2\Delta q_S^2 = (\lambda/4w)^2$ for a particle of width w, or

$$\langle I(q)\rangle_q = I_0\,P\,r_e^2\,\frac{N_{\mathrm{atom}}\lambda^2}{16w^2}\,|f|^2 \tag{9}$$

in the case where there is no sample motion during the pulse. Equations (8) and (9) assume that the positions of atoms are completely uncorrelated, which is approximately true at resolutions approaching the atomic scale. They give an estimate of average counts per pixel per particle for

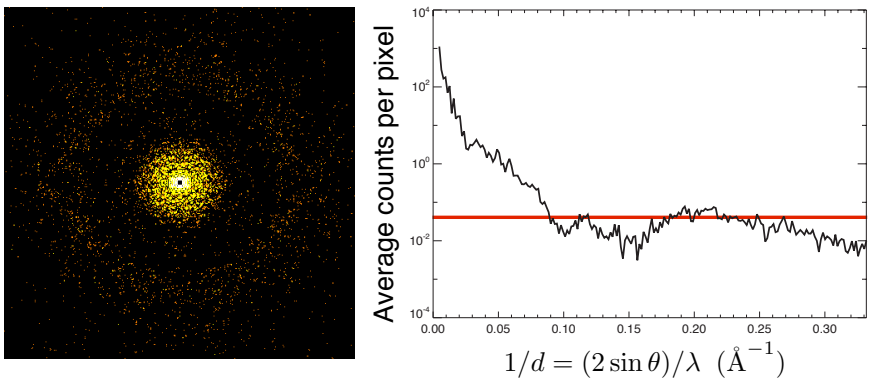

Fig. 3: *Calculated diffraction pattern of a single cow pea mosaic virus (CPMV) particle for* 10^{12} *incident photons focused to a* 0.3-μm *diameter spot, at 8 keV photon energy.*

a single shot. For the CPMV particle, of width $w = 31\,\mathrm{nm}$, we obtain $\langle I(q)\rangle = 0.04$ photons per Shannon pixel, indicated by the red line in the plot of Fig. 3. We see from Eqn. (9) that there is a large incentive to perform measurements at as long a wavelength as possible that can support the desired resolution, and that the scattering signal is not strongly dependent on the size of the object, since $N_{\mathrm{atom}} \propto w^3$. With this model we find that biological particles of around 10 nm diameter require a pulse fluence of 10^{13} photons/$(0.1\mu\mathrm{m})^2$ for an average of 0.1 photon per Shannon pixel at a resolution of 3 Å and a photon energy of 8 keV. For a pulse duration of 30 fs this requires the exceptionally high irradiance of $4 \times 10^{21}\,\mathrm{W/cm^2}$, the effect of which is examined in Sec. 4. At 3 keV photon energy, the required irradiance is reduced to $2 \times 10^{20}\,\mathrm{W/cm^2}$, although the increased photoabsorption cross section at this photon energy leads to faster destruction of the object. The signal level of 0.1 photon per Shannon pixel is higher than required by the averaging and assembly procedures discussed in Sec. 5.

3 Image Reconstruction

3.1 The Phase Problem

The reconstruction of a 2D or 3D image of the electron density $\rho(\mathbf{x})$ requires the inversion of Eqn. (7). While the modulus of the Fourier amplitudes can be obtained from $\sqrt{I}(\mathbf{q})$, the phases are missing. That is, we know the strength $|\tilde{\rho}|$ of each volume grating (of a specified period and direction given by $\mathbf{q}$) in the image, but not how these gratings are shifted with respect to each other. If the phases are known then the synthesized image is a coherent sum of these properly positioned frequency components, which is simply the inverse Fourier transform of $\tilde{\rho}(\mathbf{q})$:

$$i(\mathbf{x}) = \mathcal{F}^{-1}\{\tilde{\rho}(\mathbf{q})\} \equiv \int \tilde{\rho}(\mathbf{q}) \exp(-i\mathbf{q}\cdot\mathbf{x})\, d\mathbf{q}. \tag{10}$$

In the case of reconstructing an image from a single diffraction pattern, this image synthesis is the same as would be carried out by a perfect lens. The lens of course avoids the need to retrieve phases, since it acts upon the far-field wavefield incident on its pupil, and in a microscope the image intensity is directly measured, not the far-field pattern. The resolution of the lens-based image is equivalent to that retrieved from the diffraction pattern if the acceptance of the lens is

the same as the angular extent of the recorded diffraction pattern. For example, a diffraction pattern that extends to a scattering angle of 2θ will resolve spatial periods in the object as small as $d = \lambda/(2\sin\theta)$. Similarly the lens-based image (of a coherently illuminated object) has a resolution commonly expressed as $d = \lambda/\mathrm{NA} = \lambda/\sin(2\theta)$, where NA is the numerical aperture of the lens.

Note that just having a detector of large angular extent does not necessarily guarantee a high-resolution image. The high-angle diffraction data of course must be detected above noise. The same is indeed true for a lens-based microscope, where the resolution of the image might not fulfill that expected by the numerical aperture of the lens. An estimation of the resolution in an X-ray or electron microscope is obtained by examining the Fourier spectrum of the recorded image. For our "lensless" imaging method we can look directly at the recorded diffraction pattern, although the resolution of the image will depend upon the reliability of the phases obtained. Methods of estimating this from the reproducibility of retrieved phases have been developed [13], but this does not necessarily mean the phases are the correct ones. Perhaps the most satisfactory way of estimating resolution is based on comparing images (or diffraction phases) retrieved in separate measurements, as is common in crystallography and single-particle electron microscopy.

The coherent X-ray diffraction data in Fig. 2 contains $512 \times 512 \times 512$ pixels, or measurements of Fourier amplitudes, $\sqrt{I}(\mathbf{q})$. Inversion to an image in this case requires the recovery of over 10^8 phases. The retrieval of these phases depends upon the observation that the number of independent measurements may exceed the number of degrees of freedom describing the image. A much simpler example is the diffraction pattern of a pair of point scatterers, separated by a distance w, and measured to a resolution $q_{\max} = 2\pi/d$. In one dimension there are only four values to describe this object: the distance between the points, the moduli of the scattering strengths of both points, and the relative phase between them. From Eqns. (4) and (7) the diffraction pattern is a fringe pattern

$$I(\mathbf{q}) \propto |\tilde{\rho}(\mathbf{q})|^2 = \left|a_1 e^{i\phi_1} + a_2 e^{i\phi 2}\, \exp(i\mathbf{w}\cdot\mathbf{q})\right|^2 = a_1^2 + a_2^2 + 2a_1 a_2 \cos(wq - \phi_1 + \phi_2), \quad (11)$$

which has a period $q_p = 2\pi/w$ and a contrast $(I_{\max} - I_{\min})/(I_{\max} + I_{\min}) = 2a_1a_2/(a_1^2 + a_2^2)$. The fringe pattern is also shifted from the origin by the phase difference $\phi_1 - \phi_2$. The measurements of these quantities, and the overall strength of the diffraction pattern is enough to retrieve the amplitudes of the scatterers although there is an ambiguity in the sign of the phase difference and in which point has amplitude a_1. In this example, the number of measurements matches the number of degrees of freedom in the image (ignoring the trivial differences just mentioned). Consider now an object consisting of three points in a row, each separated by w. This will give diffraction fringes spaced by $2\pi/w$ due to interference between the scattering from the extreme points, as for the two-point case, and also at half that period, π/w, from interference of scattering from neighboring points. In this case it is not possible to uniquely assign the strengths and phases of the points. For example, the two objects $O_1 = \{1, 4, 4\}$ and $O_2 = \{2, 5, 2\}$ have equal diffraction patterns, where the three values are the scattering amplitudes of the three equally-spaced points (see Fig.4 (a)). In fact, the 3-point problem generally has two solutions, since $\{1, a+b, ab\}$ and $\{a, 1+ab, b\}$ generate the same pattern. Therefore, image reconstruction is not generally unique in one dimension. In two dimensions it has been shown that the solution is most likely unique, except for rare and special cases [14]. This is essentially due to the fact that for each line in a 2D image there are orthogonal line images that constrain the image values. For example 5-point 2D objects constructed from the sequences O_1 or O_2 can be distinguished from each other through the difference in strength of the diagonal fringes in the patterns as

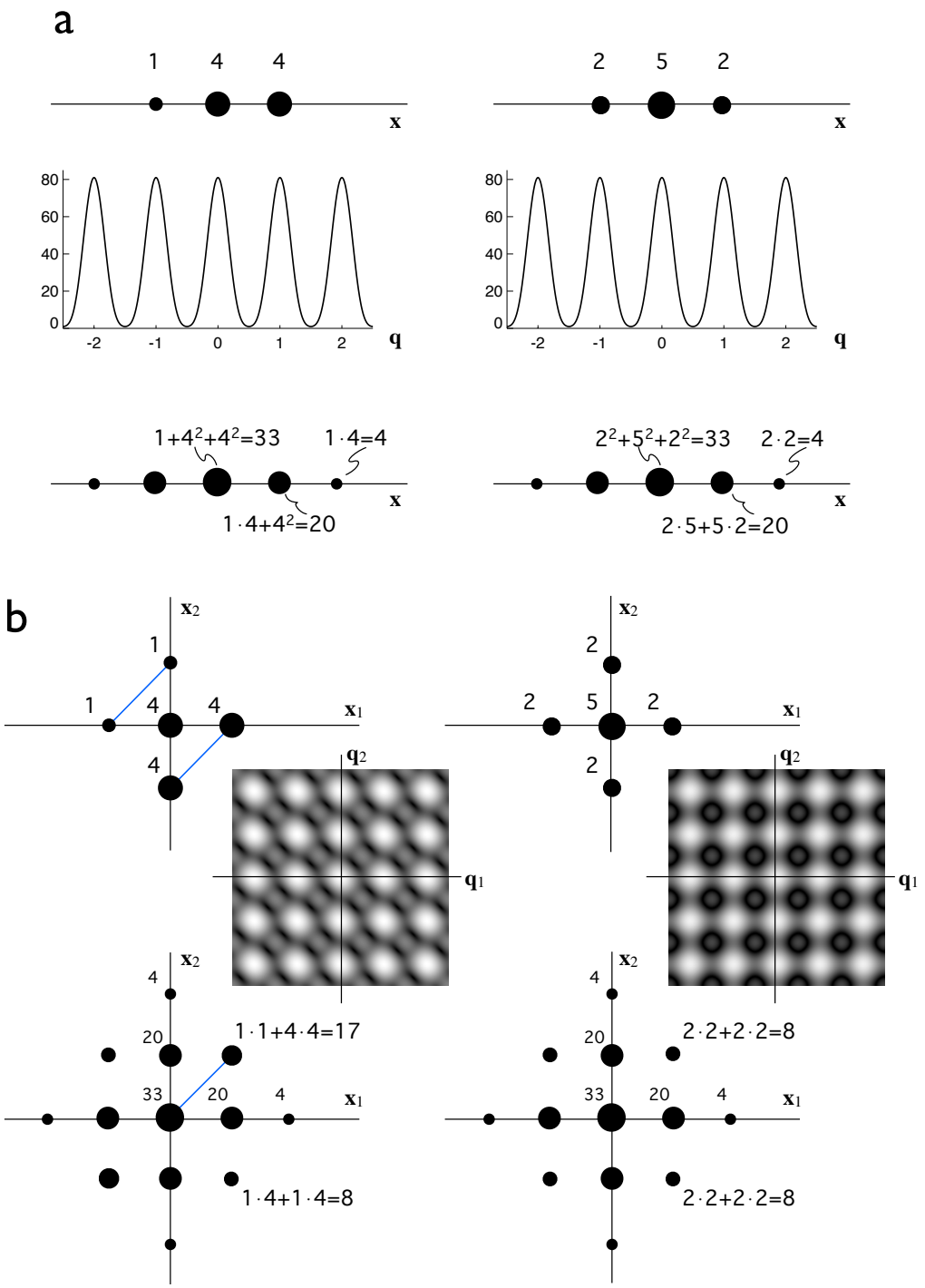

Fig. 4: *(a) Two different 3-point objects (top) have the same 1D diffraction pattern (center) and spectrum of diffraction intensities (or autocorrelation) (bottom). (b) This equivalence is broken by interference between objects in different directions, introduced in two or more dimensions.*

shown in Fig. 4 (b). While it may be possible to construct two or more 5-point 2D objects with the same pattern, these are unusual cases. Image reconstruction is even more robust in three dimensions.

The frequencies in the intensity pattern are represented by *its* Fourier spectrum $\tilde{I}(\mathbf{x})$. This real-space function is proportional to $\mathcal{F}^{-1}\{|\tilde{\rho}(\mathbf{q})|^2\} = \rho(\mathbf{x}) \otimes \rho^*(-\mathbf{x})$, the autocorrelation of the electron density (as obtained from object spatial frequencies on the Ewald sphere in the case of a single coherent diffraction pattern). We saw in the case of the two-point object that the diffraction pattern consists of just two frequencies: the zero frequency (a dc term) and one of period $2\pi/w$. $\tilde{I}(\mathbf{x})$ gives the phase and amplitude of these frequencies, as well as the negative frequency which adds no further information since $\tilde{I}(\mathbf{x})$ is Hermitian, $\tilde{I}^*(-\mathbf{x}) = \tilde{I}(\mathbf{x})$. The image retrieval problem is equivalent to finding a compact function $\rho(\mathbf{x})$ from its autocorrelation function. Each sampled $\tilde{I}(\mathbf{x})$ is dependent on all pairs of image points whose positions differ by the vector $\mathbf{x}$.

The simple examples of the point objects illustrates some of the requirements in measuring diffraction data and hints at how the missing phases are encoded in the diffraction pattern. An object of maximum width w will give rise to fringes of finest period $2\pi/w$ in the diffraction pattern. The diffraction pattern is therefore band-limited, and from Shannon's sampling theorem the complete intensity field is determined from greater than two equally-spaced samples for every $2\pi/w$ period: $\Delta q > \Delta q_S = \pi/w$ (where we refer to Δq_S as the Shannon sampling interval). Collecting samples at finer intervals than π/w does not provide any more information (although in practice there are reasons to do so, discussed below). For a resolution $q_{\max} = 2\pi/d$, there are $N_S = 2q_{\max}/\Delta q_S = 4w/d$ Shannon samples (if the diffraction pattern is measured from $-q_{\max}$ to $+q_{\max}$). The Shannon sampling interval in real space is $\Delta x_s = d/2$, and so the minimum real-space field of view that can be retrieved from adequately-sampled diffraction data is $N_S\,\Delta x_s = 2w$, twice the width of the compact object. The diffraction pattern from a general 1D complex-valued object of width w will consist of $N_S = 4w/d$ independent measurements, for a resolution of d. The number of degrees of freedom in the complex-valued image is $2w/\Delta x_s$ (a real and imaginary value per each of the $w/\Delta x_s$ real-space samples). This is exactly equal to the number of Shannon samples in the pattern, which is a necessary condition to retrieve a unique image (although, as demonstrated above, not a sufficient condition). In 2D, an object of square support of width w gives rise to N_S^2 independent measurements in its diffraction pattern, needed to recover $2(w/\Delta x_s)^2 = N_S^2/2$ image coefficients. In 3D there are four times as many independent measurements as unknowns. Another way of viewing this is that the region in real space that is constrained becomes a larger fraction of the sampled space as the number of dimensions increases: outside the support we know that the image amplitude is zero.

The ratio Ω, of the number of independent measurements to the number of independent image coefficients, appears to be a good indicator of the ability to reconstruct the image [15]. The shape of the object's support can increase this overdetermination ratio, with non-convex shapes and those without centrosymmetry leading to higher values. For example a triangle support gives $\Omega = 3$ in 2D, compared with $\Omega = 2$ for a square. Objects with well-separated components are generally easier to reconstruct. A 2D object support consisting of two squares of width w with their center points separated by $> 2w$ has $\Omega = 3$ since the autocorrelation support consists of three squares of width $2w$. The ratio Ω is increased further when when one of the components is smaller than the other, approaching the case of Fourier transform holography as one of the components approaches a delta function (see [16]). The autocorrelation vectors of magnitude greater than the width of either of the components must be due to pairs of image points in separated components, which further constrains the reconstruction.

Note that a crystal consisting of identical objects arranged in a cubic lattice of width w gives rise to Bragg peaks separated by $\Delta q_B = 2\pi/w$, which is twice the Shannon sampling rate Δq_S (the underlying molecular transform is under sampled in each dimension by a factor of 2 relative to the Shannon rate). In this case the number of unknowns to be retrieved is twice the number of independent measurements in 3D, $\Omega = 1/2$, which explains why solving the phase problem for crystals is more difficult than for non-periodic objects. Non-crystallographic symmetry (where two or more copies of a molecule occur in the crystal which are not related by the symmetry of the lattice) and changing the unit cell parameters by swelling are two methods to increase the number of independent measurements to improve phasing efforts. In many cases the molecule does not fill the entire volume of the unit cell and the smooth solvent region reduces the number of coefficients to recover. In large complexes this solvent volume can reach as high as 80%, which would increase Ω from $1/2$ to 1.25 (if the support of the molecule was known). In other instances, some proportion of the molecular structure may be known (e.g. an unknown drug fragment bound to a known target), which may significantly change the balance of known parameters to retrieved phases.

3.2 Iterative Phase Retrieval Algorithms

Reconstructing an image from a coherent diffraction pattern of an isolated object requires retrieving the diffraction phases, utilizing the constraint that the real-space image $\rho(\mathbf{x})$ is zero outside its support, plus any other constraints that can be applied. Iterative algorithms successively apply operators with the aim to converge to the image which is contained within the support and whose Fourier spectrum matches the measurement.

The simplest iterative scheme is Fienup's Error Reduction (ER) algorithm [8], which begins from the square root of the measured diffraction intensities and a random guess of the phases: $\tilde{\rho}'_1(\mathbf{q}) = \sqrt{I}(\mathbf{q}) \exp\{i\phi(\mathbf{q})\}$. The image $\rho'_1(\mathbf{x})$ is then formed by an inverse Fourier transformation. This image will not be zero everywhere outside the actual support S of the object. The estimate $\rho_2(\mathbf{x})$ is obtained by setting $\rho'_1(\mathbf{x})$ to zero outside S. This is transformed to $\tilde{\rho}_2(\mathbf{q})$ which will no longer be in agreement with the measured Fourier amplitudes. An update is formed by setting $\tilde{\rho}'_2(\mathbf{q}) = \sqrt{I}(\mathbf{q}) \exp\{i\phi_2(\mathbf{q})\}$, where $\phi_2(\mathbf{q})$ are the phases from $\tilde{\rho}_2(\mathbf{q})$. This procedure is then iterated, ideally until both sets of constraints are satisfied.

The image can be represented by a vector in an N-dimensional vector space, where N is the number of pixels (or voxels) in the image. The complex amplitude at each pixel gives the value of the vector along each corresponding dimension. In this representation the ER algorithm can be written as

$$\rho_{n+1}(\mathbf{x}) = P_S \, P_M \, \rho_n(\mathbf{x}) \tag{12}$$

where the projection operators are given by

$$P_S \, \rho(\mathbf{x}) = \begin{cases} \rho(\mathbf{x}) & \text{if } \mathbf{x} \in S \\ 0 & \text{otherwise.} \end{cases} \tag{13}$$

and

$$\tilde{P}_M \, \tilde{\rho}(\mathbf{q}) = \sqrt{\frac{I(\mathbf{q})}{|\tilde{\rho}(\mathbf{q})|^2}} \, \tilde{\rho}(\mathbf{q}) \tag{14}$$

with

$$P_M = \mathcal{F}^{-1} \, \tilde{P}_M \, \mathcal{F}. \tag{15}$$

Projection operators have the property that $P^2 = P$. Error metrics describing how well the modulus and support constraints are satisfied can be expressed as Euclidean distances $\epsilon_S = \|P_S\rho - \rho\|$ and $\epsilon_M = \|P_M\rho - \rho\|$, respectively, where $\|\cdot\|$ is defined as the sum of the square moduli of the vector components. It is clear from these definitions that an iteration of $P_S\,P_M$ will always decrease the errors ϵ_S and ϵ_M, which is why Fienup called this the Error Reduction algorithm. However, this algorithm has no method to escape from local minima, which would require a step that increases these metrics. Numerous algorithms have been proposed to overcome the stagnation problem inherent in the ER algorithm, of which the most popular is the hybrid input-output (HIO) algorithm [8], which can be expressed as

$$\rho_{n+1}(\mathbf{x}) = (P_S\,P_M + (I - P_S)(I - \beta P_M))\rho_n(\mathbf{x}), \tag{16}$$

in the case when a only a support constraint is applied in real space. Inside the support, where $(I - P_S)\rho = 0$, the modulus constraint is applied as in the ER algorithm. Outside the support, instead of setting ρ to zero to exactly satisfy the support constraint, the iterate ρ_{n+1} is formed by subtracting $\beta P_M\,\rho_n$ from ρ_n, where β is a constant usually in the range 0 to 1. The inspiration for this algorithm comes from control theory, with the idea to provide a negative feedback to the operation of applying the modulus constraint. The input to P_M is compensated at those points where the support constraint is violated. This allows the algorithm to escape local minima. Often several iterations of ER are inter-dispersed between HIO steps. Other algorithms improve the convergence rate by taking bigger steps in image space or altering the search strategy, as explained and reviewed by Marchesini [17].

Iterations proceed until the error metrics converge. The final iterate is not necessarily equal to the solution, $\bar{\rho}$, which is the intersection of the two sets, $\bar{\rho} = P_S\bar{\rho} = P_M\bar{\rho}$ [18]. The solution can be found from $\bar{\rho}(\mathbf{x}) = P_M\,\rho_n(\mathbf{x})$. Due to measurement noise a single true solution cannot be distinguished from a family of images that satisfy all constraints to within the the errors. An average solution can be determined by continuing the iterations and generating solutions say every 100 iterations, or by rerunning the algorithm from random phases [19]. This average is unique, and is perhaps the best estimate of the true image that could be obtained from the data. The procedure also allows us to determine the reliability of the retrieved phases. Diffraction phases that always reconstruct to the same value will add complex amplitudes constructively, whereas the sum of amplitudes with random phases will tend to zero. By comparing the modulus of this average to the square root of the measured diffraction intensities we obtain a value at each diffraction pixel that is < 1 and only equal to 1 when phases are exactly consistent. This value tends to decrease with increasing resolution due to the fact that diffraction amplitudes decrease with resolution and are more influenced by noise. This ratio indicates how well the spatial frequencies of the image are represented in the phasing process and is accordingly referred to as the phase retrieval transfer function (PRTF). The average solution can be thought of as the true solution imaged through an optical system with a transfer function given by the PRTF. When performing the average the constant phase term must be normalized to the same value for each solution, otherwise the PRTF will be < 1 for the zero frequency (representing an attenuating optical system). Other low-order aberrations including wavefront tilt (displacement of the image), defocus, and Seidel aberrations such as astigmatism and coma, can also be removed from each solution before determining $\langle\bar{\rho}\rangle$. Since these types of aberrations only cause blurring or shifting of the image, they are not fully constrained by a loose support, unless a positivity constraint is applied (the out of focus image of a positive-density object will have negative amplitudes) [20].

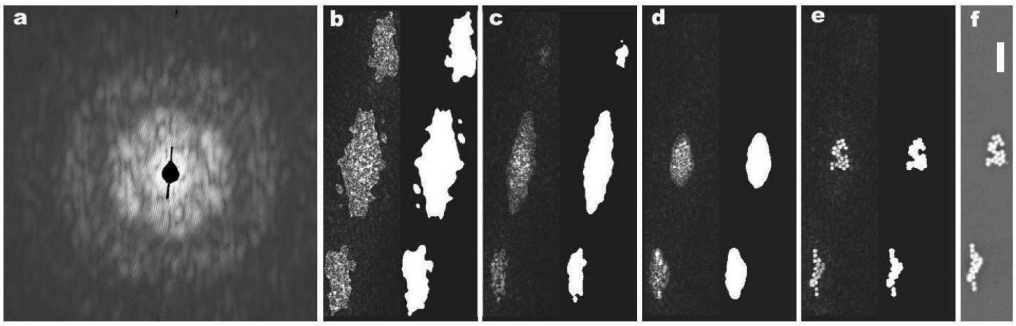

Fig. 5: *Image reconstruction from the coherent diffraction pattern in (a). The process starts from zero phases, giving the autocorrelation of the image, in (b). The first support is obtained by a threshold of this image. As phase-retrieval iterations proceed the support is re-estimated, as shown in (c) to (e). An SEM image of the object is in (f). From [5].*

When imaging at hard X-ray wavelengths away from atomic resonances, or imaging binary objects at any wavelength, a positivity constraint can be applied to the real-space image values. With soft X-rays (photon energies below about 1 keV) most interesting objects are complex valued. In this case, a successful reconstruction requires a support constraint that closely matches the actual boundary of the object, since with a loose support an out-of-focus image would be a valid solution. However, it is unlikely that the support is known to such accuracy. Marchesini noticed that the tighter the support constraint the better the reconstruction, leading him to propose the Shrinkwrap method [5]. As illustrated in Fig. 5 this adds a dynamic support constraint to an iterative transform algorithm, where the support is updated occasionally based on the current reconstruction. Image pixels below a certain threshold of a blurred version of the current reconstruction are treated as being outside the object. Starting from the support of the image autocorrelation, the support tends to gradually shrink to the boundary of the object, improving the reconstruction as it does so (which then gives an improved estimate of the support). A stopping criterion must be added otherwise the method tends to over shrink; when this happens the error ϵ_S increases abruptly, allowing this transition to be determined.
In many experimental situations, especially single-shot imaging at X-ray free-electron lasers, there are missing data at low scattering angles near the zero-order beam. Unless the sample has been designed to be mostly absorbing (as can be achieved in imaging magnetic domains in thin films, for example) the zero-order beam will be extremely intense, and is usually managed with a beam stop or a hole in the detector. If this missing region is as small as a single speckle, only the overall scattering strength of the object is lost. As this region increases more information is lost, often causing iterative algorithms to fail. When only a support constraint is applied, there will be particular modes that are neither constrained by the diffraction measurement nor the support [19]. However, it is possible to reconstruct images missing these low frequencies, just as a lens with an annular pupil will give rise to high-pass filtered images [21].

3.3 Coherence and Detector Requirements

Reconstructing images of non-periodic objects from their X-ray diffraction patterns has been found to be more problematic than experienced in computer simulations or visible light experiments. This may be due to the fact that most X-ray experiments have been carried out with

partially-coherent beams. The van Cittert-Zernike theorem states that the mutual coherence function of a beam propagating from an incoherent source is given by the Fourier transform of the source intensity distribution. Application of this theorem to an object illuminated by this partially-coherent beam shows that its far-field diffraction pattern is given by

$$I(\mathbf{q}) = |\tilde{\rho}(\mathbf{q})|^2 \otimes p(\mathbf{q}) \tag{17}$$

where p is the spatial distribution of the source, such that its angular extent is given by $p(4\pi\theta/\lambda)$. More generally, in the Gaussian-Schell model the source can described in terms of mutually incoherent modes and the diffraction pattern is then the sum of intensity patterns arising from each mode. The image reconstruction as described in the previous section assumes full coherence, with $p(\mathbf{q}) = \delta(\mathbf{q})$. As can be seen from Eqn. (17) the effect of the source is to reduce the contrast of the diffraction pattern, and in particular causing the zeroes in the intensity pattern to have positive values. This causes problems in assigning phases to the values $\sqrt{I(\mathbf{q})}$ since there will be a discontinuity from negative to positive diffraction amplitudes.

The effect of the finite width of detector pixels is also a convolution, given by Eqn. (17), where $p(\mathbf{q})$ is now the pixel sensitivity. The decrease in fringe contrast in the diffraction pattern causes a modulation of the autocorrelation by the function $\tilde{p}(\mathbf{x})$, the modulation transfer function of the detector or the mutual coherence function of the source. The width of this function (i.e. the transverse coherence length) must be significantly wider than the width of the object autocorrelation, or twice the largest diameter of the object. For example, a square-pixel detector that is fully sensitive across its area (which is approximately the case for CCD detectors) will not detect the finest fringes in the pattern when the pixel spacing matches the Shannon sampling rate. That is because a pixel integrates over half a period of these finest fringes, which will be exactly equal to the integration over the other half period in its neighboring pixel. Improved estimates of the Shannon samples are obtained by increasing the pixel density.

Often the function p can be estimated or measured so that the diffraction pattern contrast can be corrected. This deconvolution is carried out by dividing the autocorrelation $\tilde{I}(\mathbf{q})$ by the MTF $\tilde{p}(\mathbf{q})$, a high-pass filtering operation. Since this deconvolution procedure can amplify noise, following Whitehead *et al.* [22] we could propose to *convolve* the current iterate with p before comparing with the measurement to update the modulus of $\tilde{\rho}$, by replacing Eqn. (14) with

$$\tilde{P}_M\, \tilde{\rho}(\mathbf{q}) = \sqrt{\frac{I(\mathbf{q})}{|\tilde{\rho}(\mathbf{q})|^2 \otimes p(\mathbf{q})}}\, \tilde{\rho}(\mathbf{q}). \tag{18}$$

In this way the moduli are updated by first computing the partially-coherent diffraction pattern that would arise from the current estimate of $\rho(\mathbf{x})$, and comparing this with the measurement $I(\mathbf{q})$. Equation (18) is not a projection operator, since repeated application may continue to change ρ. The modal method for reconstruction of images from partially-coherent diffraction patterns derived by Whitehead *et al.* [22] has nevertheless been found to substantially improve the success of image reconstructions using experimental data. When the width of p is small enough that the highest period fringes discerned in the pattern are due to the most distant inter-object separation, then even rough estimates of p lead to improved reconstructions.

The assumption of quasi-monochromaticity inherent in the discussion up until now requires a bandwidth spread $\Delta\lambda/\lambda < 1/N_S$. This condition can be relaxed if the spectrum is known such that the polychromatic diffraction pattern due to the current estimate of $\rho(\mathbf{x})$ can be calculated [23], in a similar treatment to partial spatial coherence. Additionally, the framework of partial coherence can be applied to changes in the sample itself, either due to X-ray induced damage [24] (and see below) or sample motion [25].

4 Outrunning Radiation Damage

4.1 Diffraction Before Destruction and Time-Delay Holography

As mentioned in the Introduction, recording diffraction from non-crystalline material requires a vastly greater exposure than required for crystalline material. The limitation to acquiring high-resolution diffraction information is due to radiation damage: the very radiation used to determine structure impairs that structure. The dose (energy per unit mass) that cryogenically cooled biological material can withstand is about 30 MGy before changes are observed in the molecular constituents of the sample. By using pulses shorter than the timescale of radiation damage processes, we can literally outrun damage and increase the dose by many orders of magnitude [11]. With short-pulse X-ray FEL radiation at high irradiance (10^{18} to 10^{21} $\mathrm{W/cm^2}$ or doses up to 100 GGy at 8 keV photon energy) the high degree of ionization of every atom in the sample will cause an isolated object to Coulomb explode, yet the inertia of atoms provides on the order of 10 fs before atomic displacements will significantly alter the diffraction pattern at atomic resolutions. The electron density of ions is of course lower than neutral atoms, and this ionization will also give rise to modification to the pattern even before atomic motion occurs. The random occurrence and sequence of ionization will on average cause an uncorrelated (that is, q-independent—at least at low resolution) addition of diffuse diffraction and reduce the overall contrast. This method of "diffraction before destruction" was first demonstrated at the FLASH FEL at soft X-ray wavelengths [26], and has now been verified to hold at atomic resolution [27], and the processes of radiation damage over the timescale of the pulse is an active area of experimental and theoretical research.

Since initial FEL experiments were limited to long wavelengths (and hence low spatial resolution), essentially no damage could be observed over the limited duration of the pulse [26]. The effects of the X-ray pulse on the material could only be discerned by tracking the explosion at tens of nanometre length scales taking place on picosecond timescales. This was carried out by an interesting method dubbed time-delay holography [28]. After interacting with the sample, the pulse is reflected by a normal-incidence multilayer mirror back onto the sample to diffract again. The initial (prompt) diffraction is also reflected in the mirror. This and the delayed diffraction propagate together to a diffraction camera located in a backscattering geometry (the incident beam passes through a hole in this detector on the way to the sample). The time delay between the pulse passing through the sample for the first and second times is given by $2\ell/c$ where ℓ is the distance from sample to mirror and c the speed of light. In experiments this was varied from 350 fs to several picoseconds. The two diffraction patterns interfere at the detector since there is zero path difference between the light that diffracts first from the sample then reflects and the light that reflects first from the mirror then diffracts. Unfolding the effect of the mirror shows we are diffracting from two objects longitudinally displaced a distance 2ℓ from each other. Two point sources in this configuration give rise not to straight fringes, but circular fringes with a spacing that decreases with the square of scattering angle (the center of the circles is on the line passing through both objects, i.e. normal to the mirror). Such a pattern is convolved with each scattering point in the sample. The fringes precisely encode the time delay, and the prompt diffraction (from the known undamaged object) acts as a holographic reference to help retrieve an image of the exploding object. A shift of the fringes gives an interferometric measurement of the change in refractive index of the object, which was used to determine that the expansion of a latex microsphere test object was less than 6 nm in 350 fs. The idea for this experiment was inspired by an exhibit of Newton's dusty mirror at a science museum where

circular fringes could be observed (in visible light) from spores dusting the front surface of a back-silvered mirror. Newton first observed and described interference via this arrangement, although Thomas Young was the first to interpret the observations correctly. Our method of reflecting the same pulse onto the sample to examine it at a precise later time was also used to confirm predictions that a sacrificial layer around an object (a tamper) delays the explosion of that object [29].

4.2 Diffraction Termination

Molecular dynamics calculations can give detailed simulations of the X-ray induced explosion that take into account the initial molecular structure of samples. These calculations are computationally expensive, and so are limited to small samples such as single macromolecules. A continuum approach applies methods developed to model dense plasmas such as in stellar interiors (somewhat larger than a molecule), but makes the assumption that in small regions the dynamics of the sample are isotropic. A code called Cretin was used to simulate the structural changes at atomic resolution in small protein crystals of about $1\,\mu\mathrm{m}$ diameter, embedded in a water tamper [12]. The calculations make discrete time steps in which the atomic populations and electron and photon distributions are calculated utilizing known transition rates and opacities. These provide electron and ion temperatures, ionization states and ion collisions, from which mean atomic displacements are computed, as shown in Fig. 6. The RMS displacements are obtained from a diffusion equation where the diffusion coefficient is calculated from the ion collision frequencies and temperatures. As seen in the figure the RMS atomic displacement σ increases approximately as $t^{3/2}$ over the time t of a constant-irradiance pulse. The explosion occurs faster for higher pulse irradiance, with σ approximately proportional to the square root of pulse irradiance (photons/unit area/unit time) for the range of irradiance considered here. At 8 keV photon energies, this dependence continues beyond an irradiance of $10^{21}\,\mathrm{W/cm^2}$ which corresponds to focusing 10^{13} photons in 10 fs to a spot of $0.4\,\mu\mathrm{m}$ diameter. At this photon energy and irradiance, an RMS displacement of 1 Å is reached in about 10 fs.

Each X-ray induced explosion of an identical object will be different due to the random sequence of ionization and atomic displacements. The diffraction signal obtained by averaging over many instances of these explosions can be obtained through the derivation, found in several text books (see e.g. [30]), for describing small random displacements in crystals due to thermal motion. It is interesting to note that this common derivation makes no explicit assumption as to whether the almost-identical objects are arranged and exposed together (as in a crystal) or exposed in a serial fashion and diffraction intensities then summed. This is the case if there is no spatial correlation to the displacements and hence no correlation of these displacements from unit cell to unit cell (if considering a crystal), and that the RMS displacement within a single object is the same as the RMS displacement in the whole crystal. We assume that diffraction patterns are properly oriented prior to averaging, by the methods of Sec. 5. The effect of isotropic displacements is to multiply the diffraction signal at a momentum transfer q by a factor of $\exp(-q^2\sigma^2)$. Here σ is the RMS of the component of the displacement in the direction of $\mathbf{q}$, equal to the 1D component of the mean displacements for isotropic displacements, as plotted in Fig. 6. In our accelerating explosion, σ increases during the exposure. The instantaneous diffraction signal at a resolution d is reduced by $1/e$ when σ reaches a value of $d/(2\pi)$. Displacements of only 0.5 Å terminate the accumulation of intensities at 3 Å resolution. The summed diffraction signal from recorded patterns is the pulse-integrated signal. Following

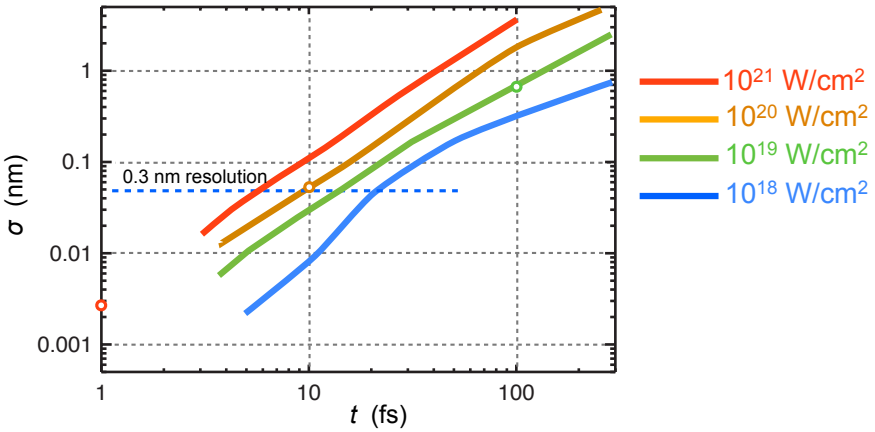

Fig. 6: *Plot of the RMS isotropic atomic displacement σ as a function of time t during pulses of constant irradiance as shown in the legend, for a photon energy of 8 keV. The open circles indicate the time required to reach a fluence of 10^6 J/cm^2 as in the simulation of Fig. 3, showing that higher pulse power (photons per unit time) gives less damage for a given total scattering signal. Lower resolution can tolerate longer (and therefore less intense) pulses. From [12].*

Eqn. (7) this diffraction signal for a constant irradiance pulse of duration T is given by

$$I(\mathbf{q}) = I_0\, T\, \Omega_p\, P\, r_e^2\, \left\{ |\tilde{\rho}(\mathbf{q})|^2\, g(q;T) + N_{\rm atom} |f|^2 (1 - g(q;T)) \right\}, \tag{19}$$

$$g(q;T) = \frac{1}{T} \int_0^T \exp\{-q^2 \sigma^2(t)\}\, dt. \tag{20}$$

Here we have omitted another multiplicative Wilson factor of $\exp(-Bq^2/8\pi^2)$ to describe the structure variation inherent in the unexposed samples, and note that the total incident fluence is given by $I_0\, T$ (in units of photons per unit area).
Equation (19) consists of two terms. The first is the undamaged diffraction pattern $|\tilde{\rho}(\mathbf{q})|^2$ modified by the dynamic disorder factor $g(q;T)$, a function that decreases monotonically with increasing q. The second term is a slowly-varying background of scattered counts that is proportional to the overall scattering strength of the sample and which increases monotonically with increasing q. This term is 0 at $q = 0$. Thus, in general, the disordering takes scattered counts out of the information-containing Shannon samples into a background that diminishes the contrast. This occurs first at high q and works its way towards lower resolution with time. Applying the empirical time dependence observed in Fig. 6 of $\sigma(t) = \sigma_T \cdot (t/T)^{3/2}$, with σ_T the RMS displacement at the end of the pulse, we find

$$g(q;T) = \int_0^1 \exp(-q^2 \sigma_T^2 t'^3) dt' = \frac{\Gamma(4/3)}{(q^2\sigma_T^2)^{1/3}} - \frac{1}{3} E_{2/3}(q^2\sigma_T^2) \tag{21}$$

where $E_{2/3}(x)$ is the exponential integral function of order $2/3$, and which tends to zero as the argument x increases, and $\Gamma(4/3) = 0.89$. That is, for high resolution $g(q;T) \approx (q\,\sigma_T)^{-2/3}$.
The behavior of g can perhaps be better understood from Eqn. (20). At early times in the pulse $\sigma(t)$ is small and the instantaneous disorder factor (the integrand) is close to unity and the diffraction pattern, proportional to $|\tilde{\rho}(\mathbf{q})|^2$, continues to accumulate. When σ reaches a value of $1/q$ this accumulation stops and the background then accumulates. This happens at a

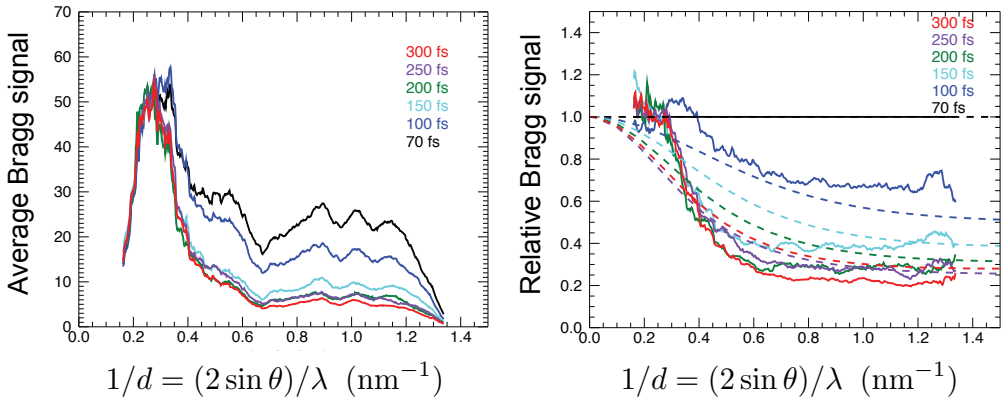

Fig. 7: *(left) Average Bragg signal of Photosystem I micro crystals as a function of resolution for different pulse durations for pulse irradiance up to* $10^{17}\,\mathrm{W/cm^2}$ *at a photon energy of 2 keV. (right) The ratio of the average Bragg signal to that at the shortest pulse duration, and comparison to ratios of the dynamic disorder factor* $g(q;T)$ *obtained from continuum modeling of the evolution of the RMS atomic displacements as shown in Fig. 6. From [12].*

time t_{off} such that $1/q = \sigma_T(t_{\mathrm{off}}/T)^{3/2}$, or $t_{\mathrm{off}} = (q\,\sigma_T)^{-2/3}\,T$. The proportion of the pulse that contributes to the cooperative diffraction is given by t_{off}/T, in agreement with the limiting value of the integration of Eqn. (21). Pulses longer than t_{off} do not contribute any more information at resolutions of q or better, and simply accumulate background for the rest of the pulse.
Our analysis suggests that the source metric to maximize signal acquisition is not the total pulse fluence, but the pulse irradiance (or source power, considering that the spot size is essentially dictated by focusing optics). If we simply increase the pulse energy (number of photons) by proportionally increasing the pulse length, then we only increase the background without improving the signal. Increasing the irradiance increases the rate of signal photons arriving on the detector but does shorten the time t_{off} that these photons accumulate. However, given the linear dependence of σ_T^2 on pulse irradiance observed in Fig. 6 we find that the total signal scales as $I_0\,t_{\mathrm{off}} \propto I_0^{2/3}$. However, if irradiance is scaled higher than $10^{21}\,\mathrm{W/cm^2}$ (at 8 keV photon energy) we can expect almost every electron to be stripped from every atom in the sample. In this case the turn-off time of diffraction will not be necessarily limited by atomic motion, but the variability in the atomic scattering factors at undisplaced atomic positions. This has no spatial correlation, and leads to a diffuse background that is independent of q and a corresponding uniform decrease in the signal. In this case, our q-independent turn-off time will depend on the atomic relaxation processes, which are not much longer than several femtoseconds.

4.3 Bragg termination

Among the first experiments to be carried out at the LCLS, the world's first hard X-ray FEL [1], was to measure the effect of pulse duration and fluence on coherent diffraction patterns. The samples chosen for confirming "diffraction before destruction" and mapping out the behavior of diffraction termination were protein nanocrystals flowing in a water jet. These are biological material and are confined in a water medium, as per the system modeled in Fig. 6. The crystallinity gives a great advantage that the diffraction signal $|\tilde{\rho}(\mathbf{q})|^2$ is confined to Bragg

peaks, whereas the background due to the explosive disordering varies very slowly across the detector. The presence of discernible Bragg peaks indicates that structure at a particular length scale persisted for some fraction of the pulse. Indeed, the measurement of the Bragg intensities as a function of pulse duration allowed us to determine this fraction, and hence quantify $t_{\rm off}$ and σ_T. For even small protein nanocrystals, and pulses not very much longer than $t_{\rm off}$, the disorder background is much weaker than the Bragg peaks. Therefore, for nanocrystallography it is not necessary to limit pulse durations to $t_{\rm off}$. The Bragg peaks terminate when the disorder reaches a level of $\sigma = d/(2\pi)$ for a resolution length d. The effect of the explosion is a filtering of the Bragg values by the dynamic disorder factor $g(q;T)$, which can be corrected by dividing the Bragg signal by an estimate of this function based on modeling of the explosion or from measurements at several pulse durations. In addition, the method of nanocrystallography opens up protein structure determination to samples that cannot be grown into crystals of sufficient size or quality for standard synchrotron radiation measurements or are particularly sensitive to radiation damage, making this a very attractive and important method for biological structure determination [27].

Figure 7 shows measurements of the termination of Bragg peaks as a function of resolution for different pulse durations, carried out at a photon energy of 2 keV (6 Å wavelength) on nano and microcrystals of Photosystem I. This is a large membrane complex involved in photosynthesis, and chosen for these experiments primarily because of its large unit cell and because it has proven to be a very difficult sample for conventional synchrotron measurements which required crystals several hundred microns large. As can be seen from Fig. 7 the diffraction efficiency is very much lower at high resolution for longer pulses compared with the shorter pulses, simply because only the first part of the pulse is contributing to the diffraction. Even so, the diffraction patterns with 300-fs pulses give Bragg peaks, at 1-nm resolution, that are easily measured and well above background. The model predictions contain no fitted parameters, and the agreement with the experimental results gives confidence of the predictions for atomic-resolution imaging.

5 Assembly of Diffraction Data from Identical Particles

As we have seen, the intense and extremely brief pulses from X-ray FELs solve the problem of radiation damage, but a single object only survives a single pulse. In the scattering geometries discussed here, this limits information collected in a single pulse to a two-dimensional slice (on the Ewald sphere) through the three-dimensional diffraction intensities $|\tilde{\rho}(\mathbf{x})|^2$. The acquisition of full three-dimensional information requires combining data from many copies of identical objects in different orientations. Summing data from many objects also increases the signal beyond that available in a single-shot pattern, which is limited by the number of incident photons per pulse as estimated by Eqn. 9. There are several ways in principle to acquire data from multiple particles so that scattering information can be combined into a single 3D dataset. We consider here methods in which the orientation of the particle to the frame of the laboratory is not known *a priori*, referred to by Elser as *cryptotomography* [31].

5.1 Serial Nanocrystallography

The most familiar and most successful method for increasing the diffraction signal of macromolecules and their assemblies is by forming crystals of these samples. Every copy in the crystal is oriented with respect to all others, and these are arranged in a 3D lattice which gives

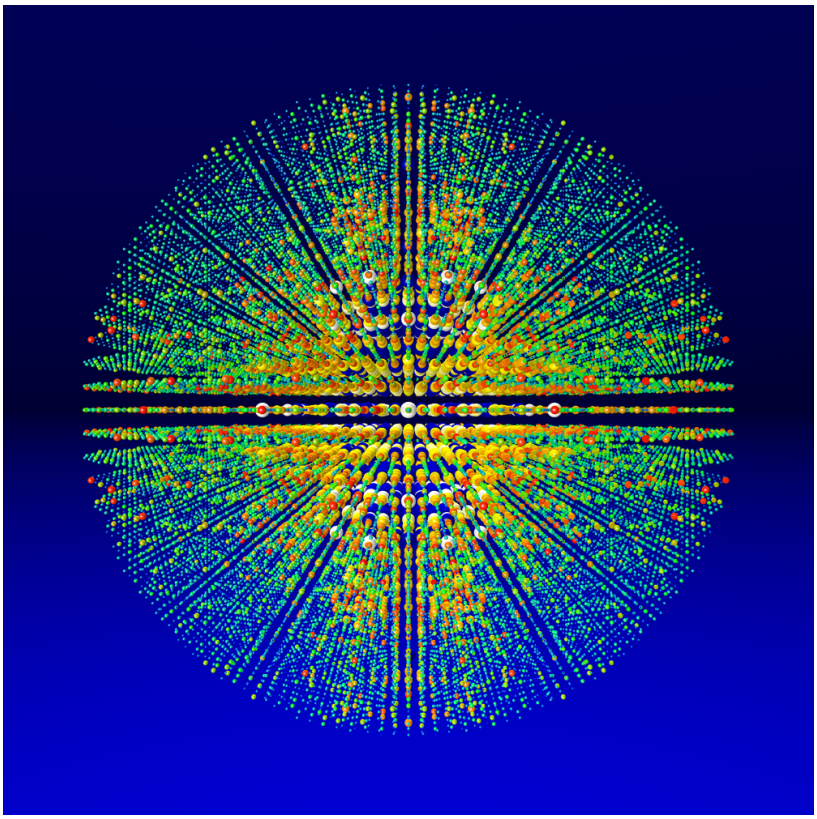

Fig. 8: *The assembled diffraction data from 56,000 nanocrystal diffraction patterns of Photosystem I collected at LCLS at a photon energy of 2 keV. Figure by Thomas White, CFEL DESY.*

constructive addition of the scattering in the particular locations of Bragg peaks. Since the real-space electron density of the crystal is a convolution of the repeated motif with a lattice, the Fourier representation $\tilde{\rho}(\mathbf{q})$ is the transform of the motif modulated by the Fourier transform of the lattice. The total integrated signal in each Bragg peak is N_{mol} times greater than that of the single particle, where N_{mol} is the total number of repeats in the crystal, and furthermore this signal is concentrated into a Fourier-space volume much smaller than the Shannon volume. For short X-ray FEL pulses, the crystalline diffraction (from structure that is correlated from unit cell to unit cell) will always give much higher counts per pixel than the disordered background. This background (which is also proportional to the total number of atoms in the crystal—see Eqn. (19)) uniformly fills the detector area between Bragg peaks whereas the peaks themselves are concentrated into approximately $1/N_{\mathrm{mol}}^{2/3}$ of the area between peaks. That is, a $10 \times 10 \times 10$ crystal will have peaks about 100 times above background when $g = 1/2$. The well-known disadvantage of crystals, mentioned in Sec. 3.1, is that the Bragg-peak spacing Δq_B is twice the Shannon spacing Δq_S for an object with the same width as the real-space lattice period, leading to fewer independent measurements than image coefficients.

In serial crystallography [27], crystals of a few micrometer or smaller are delivered to the X-ray beam in a jet of a water. A crystal is hit by chance and is situated in a random and unknown orientation. The determination of this orientation can be readily made from the pattern itself by indexing the Bragg peaks [32]. Several so-called auto-indexing programs have been developed for crystallography which search for a repeating lattice in the measured diffraction

pattern, knowing the mapping of that pattern onto the Ewald sphere. In the simple example of a monoclinic crystal with different unit cell spacings in each dimension, the reciprocal lattice basis vectors can be identified quite readily from the observed reciprocal lattice spacings and arrangement. Each Bragg peak in the pattern can thereby be indexed by its 3D Miller index $\mathbf{h}$ and thereby properly accumulated in a running sum of $|\tilde{\rho}(\mathbf{h})|^2$. In this way the diffraction data are built up, averaging over all crystal shapes and sizes, just as in the case for X-ray powder diffraction. The difference in this case is that the summation is done in three dimensions instead of the single magnitude of q, giving us complete 3D information as if collecting data from a rotating single undamaged crystal. An example of this 3D assembly is shown in Fig. 8.

5.2 Single-Particle Diffraction

Single-particle X-ray diffraction aims to carry out the same acquisition and analysis steps as for serial nanocrystallography, without the advantage of a lattice to guide us to the orientation, and without the addition of scattering from many unit cells that is concentrated into narrow Bragg peaks. It is the special case of the single-unit cell crystal. It is of particular interest because it could be applied to any series of identical objects that cannot be crystallized and allows measurement of all independent Shannon samples for the application of the phase-retrieval methods described in Sec. 3.2. The orientation analysis must be carried out on patterns with much lower signal than a single photon per pixel, as is the case for pulse energies that can be generated at X-ray FELs, such as shown in Fig. 3.

One method for determining the relative orientation of patterns is by searching for common arcs of intersection. Since every diffraction pattern samples information on an Ewald sphere that passes through the origin of Fourier space, any two patterns will always intersect along an arc that also passes through the origin. If $\rho(\mathbf{x})$ is real valued, as it is away from atomic resonances and for hard X-ray wavelengths, then $|\tilde{\rho}(\mathbf{q})|^2$ is centrosymmetric, and there will be another arc of intersection when forming the centrosymmetric inversion of one of the patterns. (Note that the diffraction pattern itself will not have centrosymmetry because the Ewald sphere is not centrosymmetric.) These two intersections allow the identification of the relative 3D orientation of the patterns. The identification of the two arcs does work even if the object density is not strictly real-valued, as shown in Fig. 9. Identifying the arcs of intersection requires a minimum signal to noise level in the patterns, which could be built up by first classifying patterns into groups of similar enough orientation that they can be summed together without knowing their relationship to other patterns. This is the approach common in the similar method in cryo-electron microscopy, where noisy real-space images are first classified into groups of similar images and then the class averages are oriented. It has been found that when working directly with diffraction amplitudes, however, that the process of correlation and orientation can be merged into one process. Recent computational experiments [34] suggest that the correlations between pairs of patterns can be made on arcs, from which a consistent set of orientations for all patterns can then be found. After arbitrarily fixing the orientation of one pattern, $N-1$ estimates of the orientation of each of the remaining $N-1$ patterns can be obtained. This procedure makes use of all correlations between pairs of patterns.

Other analysis methods for cryptotomography include the expansion-maximization-compression (EMC) framework and topological mapping [31]. The EMC method seeks to build up a model $W(\mathbf{q})$ of $|\tilde{\rho}(\mathbf{q})|^2$ by placing the two dimensional diffraction pattern measurements over a distribution of their most likely orientations. The method is iterative, starting from unknown orientation assignments. In each iteration, the model W is expanded into diffraction patterns that would

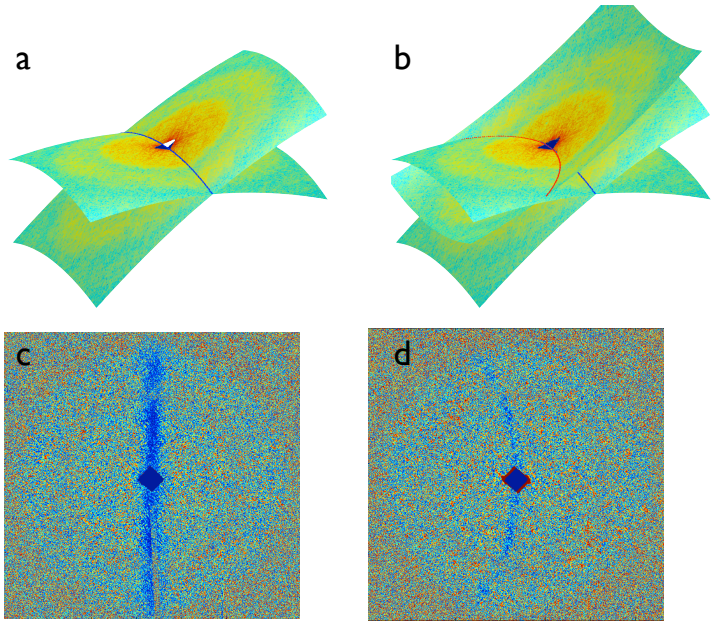

Fig. 9: *Identification of common arcs of intersection in experimental X-ray diffraction patterns taken from the same 3D nano object at two orientations. The object and diffraction data are the same as in Fig. 2. (c) shows the difference of diffraction intensities,* $I_1(\mathbf{q}) - I_2(\mathbf{q})$ *and (d) shows* $I_1(\mathbf{q}) - I_2(-\mathbf{q})$*. Figure by Gösta Huldt, Uppsala University.*

arise from such an object over a finite set of predetermined uniformly distributed orientations. The maximum likelihood step follows in which the model is changed to best agree with each of the model tomograms. In the final compression step the model tomograms are made consistent with a single updated model $W'(\mathbf{q})$. This method has successfully been applied to reconstruct the relatively simple 3D diffraction data of ellipsoidal iron oxide nano-particles measured at the FLASH FEL [33]. Elser has determined the lowest signal limits required to carry out such a procedure and finds that objects can be recovered at counts considerably less than a single photon per pixel per pattern [31]. A method that appears conceptually different (but is related [35]) is a topographic mapping approach. Utilizing the concept described in Sec. 3.2 of a diffraction pattern as a vector in a finite-dimensional vector space, it is noted that the diffraction patterns (or images) obtained at different orientations must map out a continuous 3D manifold in that higher-dimensional space. Using generative topographic mapping methods, in which this manifold is mapped out from noisy measurements, Fung *et al.* [36] recovered the structure of a molecule from simulated patterns with less than 0.04 counts per pixel.

6 Outlook

The LCLS, the first hard-X-ray FEL in the world, is now operational and many groups are carrying out new explorations into the possibilities and methodologies of imaging with brilliant coherent X-ray pulses. There is still much development needed before single-particle structure determination can be carried out routinely, but we now have strong foundations for these endeavors, as described here. All the steps for structure determination have been elucidated

theoretically with experimental confirmation. The compelling idea that the extreme irradiance of X-ray FEL pulses would allow us to obtain more information from a sample than possible at conventional sources, by virtue of outrunning the explosion caused by that high irradiance, has been examined in detail over a range of photon wavelengths, pulse durations, and fluences. These measurements give confidence that "diffraction before destruction" is valid to atomic resolution. More studies are required to determine if the dynamics of the explosion are dependent on the initial structure, especially in molecules with heavy atoms which could produce local centers of high charge that could consistently repel their surrounding atoms. However, even if there are correlated motions that occur during the explosion, the rapid destruction of cooperative diffraction by an RMS displacement of $d/(2\pi)$ due to motion of the majority of the atoms (which are of roughly equal mass) means that errors at a particular resolution will be small unless the correlated motion can be 2π times faster than the uncorrelated motion. We have found that nanocrystal diffraction is particularly impervious to the effect of the X-ray induced explosion since the diffraction from the periodic undamaged component of the structure is easily discriminated from the scattering of the disordered component. Our model of diffraction termination shows that the metric to optimize sources for imaging is pulse power. Today, the LCLS produces 50 GW X-ray pulses and designs have been proposed that could produce pulses beyond 1 TW. [37, 38].

It is straightforward to calculate the diffraction pattern of a molecular assembly (from Eqn. (7)), showing that signals at atomic resolution will invariably be at extremely low photon counts. The theoretical tools have been developed to combine data from serial measurements of identical objects to build up the three-dimensional Fourier spectrum of the average object. The experimental challenges lay in being able to actually record such weak diffraction patterns without the introduction of extraneous noise sources. Is it really possible to illuminate a macromolecular object with 10^{13} photons and yet ensure that the single photons measured in the detector pixels have scattered from that object, and are not due to scattering from optical elements, gas molecules, or other means? Once the data assembly has been accomplished, the reconstruction of a three-dimensional object is ensured by the phase retrieval algorithms that have been adequately demonstrated in many contexts. Real experimental effects such as wavelength bandwidth, spatial coherence, and detector response can all be characterized and accounted for. The phase retrieval of diffraction data sample at or beyond the Shannon rate gives an overdetermined dataset in two and three dimensions, and *ab initio* image retrieval is possible. That is, the phase problem is more easily solved than in the case of crystals, where over 50 years of insights and breakthroughs can additionally be drawn upon or adapted. For example an extension of the method of anomalous diffraction to extreme irradiance has been proposed [39].

These ideas and underpinnings have already given us a new route to obtain high-resolution room-temperature structural information from protein nanocrystals that are too small to be analyzed at conventional sources. The short pulse duration from X-ray FELs gives inherently high temporal resolution, which can be exploited in pump-probe experiments where a sample is stimulated by a short laser pulse at a precise time before the arrival of the X-ray pulse. The femtosecond pulses are over 1000 times shorter than synchrotron pulses, giving access to a full exploration of the motions involved in chemical reactions, molecular vibrations, and laser-matter interactions. The serial method can be applied to measurement of irreversible reactions. Since the sample is destroyed by the pulse anyway, there is no requirement to bring it back to the ground state as is the case for stroboscopic measurements. These experimental techniques will continue to evolve as the availability of X-ray FELs increases, providing a very bright future for X-ray imaging, in more ways than one.

References

[1] P. Emma, R. Akre, J. Arthur, R. Bionta, C. Bostedt, J. Bozek, A. Brachmann, P. Bucksbaum, R. Coffee, F. J. Decker, Y. Ding, D. Dowell, *et al.*, Nat. Photon. **4**, 641 (2010).

[2] D. Fausti, R. I. Tobey, N. Dean, S. Kaiser, A. Dienst, M. C. Hoffmann, S. Pyon, T. Takayama, H. Takagi, and A. Cavalleri, Science **331**, 189 (2011).

[3] X. Yang, Z. Ren, J. Kuk, and K. Moffat, Nature **479**, 428 (2011).

[4] D. Sayre, H. N. Chapman, and J. Miao, Acta Cryst. A **54**, 232 (1998).

[5] S. Marchesini, H. He, H. N. Chapman, S. P. Hau-Riege, A. Noy, M. R. Howells, U. Weierstall, and J. C. H. Spence, Phys. Rev. B **68**, 140101 (2003).

[6] H. N. Chapman, A. Barty, S. Marchesini, A. Noy, S. P. Hau-Riege, C. Cui, M. R. Howells, R. Rosen, H. He, J. C. H. Spence, U. Weierstall, T. Beetz, *et al.*, J. Opt. Soc. Am. A **23**, 1179 (2006).

[7] R. W. Gerchberg and O. Saxton, Optik **35**, 237 (1972).

[8] J. R. Fienup, Opt. Lett. **3**, 27 (1978).

[9] J. M. Holton, J. Synch. Rad. **16**, 133 (2009).

[10] M. R. Howells, T. Beetz, H. N. Chapman, C. Cui, J. M. Holton, C. J. Jacobsen, J. Kirz, E. Lima, S. Marchesini, H. Miao, D. Sayre, D. A. Shapiro, *et al.*, J. Elec. Spec. Rel. Phenom. **170**, 4 (2009),.

[11] R. Neutze, R. Wouts, D. van der Spoel, E. Weckert, and J. Hajdu, Nature **406**, 753 (2000).

[12] A. Barty, C. Caleman, A. Aquila, N. Timneanu, L. Lomb, T. A. White, J. Andreasson, D. Arnlund, S. Bajt, T. R. M. Barends, M. Barthelmess, M. J. Bogan, *et al.*, Nat. Photon. **6**, 35 (2012).

[13] D. Shapiro, P. Thibault, T. Beetz, V. Elser, M. Howells, C. Jacobsen, J. Kirz, E. Lima, H. Miao, A. M. Neimann, and D. Sayre, Proc. Nat. Acad. Sci. **102**, 15343 (2005).

[14] R. H. T. Bates, Optik **61**, 247 (1982).

[15] V. Elser and R. P. Millane, Acta Cryst. A **64**, 273 (2008).

[16] I. McNulty, J. Kirz, C. Jacobsen, E. H. Anderson, M. R. Howells, and D. P. Kern, Science **256**, 1009 (1992).

[17] S. Marchesini, Rev. Sci. Instrum. **78**, 011301 (2007).

[18] V. Elser, J. Opt. Soc. Am. A **20**, 40 (2003).

[19] P. Thibault, V. Elser, C. Jacobsen, D. Shapiro, and D. Sayre, Acta Cryst. A **62**, 248 (2006).

[20] S. Marchesini, H. N. Chapman, A. Barty, C. Cui, M. R. Howells, J. C. H. Spence, U. Weierstall, and A. M. Minor, IPAP Conf. Ser. **7**, 380 (2006).

[21] A. Martin, N. Loh, C. Hampton, R. Sierra, F. Wang, A. Barty, A. Aquila, S. Bajt, M. Barthelmess, C. Bostedt, J. Bozek, N. Coppola, *et al.*, *Dark-field femtosecond imaging of airborne soot with an x-ray free electron laser*, (unpublished).

[22] L. W. Whitehead, G. J. Williams, H. M. Quiney, D. J. Vine, R. A. Dilanian, S. Flewett, K. A. Nugent, A. G. Peele, E. Balaur, and I. McNulty, Phys. Rev. Lett. **103**, 243902 (2009).

[23] B. Abbey, L. W. Whitehead, H. M. Quiney, D. J. Vine, G. A. Cadenazzi, C. A. Henderson, K. A. Nugent, E. Balaur, C. T. Putkunz, A. G. Peele, W. J., and McNultyI., Nat Photon **5**, 420 (2011).

[24] H. M. Quiney and K. A. Nugent, Nat. Phys. **7**, 142 (2011).

[25] J. N. Clark, C. T. Putkunz, E. K. Curwood, D. J. Vine, R. Scholten, I. McNulty, K. A. Nugent, and A. G. Peele, Opt. Lett. **36**, 1954 (2011).

[26] H. N. Chapman, A. Barty, M. J. Bogan, S. Boutet, M. Frank, S. P. Hau-Riege, S. Marchesini, B. W. Woods, S. Bajt, W. H. Benner, R. A. London, *et al.*, Nat. Phys. **2**, 839 (2006).

[27] H. N. Chapman, P. Fromme, A. Barty, T. A. White, R. A. Kirian, A. Aquila, M. S. Hunter, J. Schulz, D. P. DePonte, U. Weierstall, R. B. Doak, F. R. N. C. Maia, *et al.*, Nature **470**, 73 (2011).

[28] H. N. Chapman, S. P. Hau-Riege, M. J. Bogan, S. Bajt, A. Barty, S. Boutet, S. Marchesini, M. Frank, B. W. Woods, W. H. Benner, R. A. London, U. Rohner, *et al.*, Nature **448**, 676 (2007).

[29] S. P. Hau-Riege, S. Boutet, A. Barty, S. Bajt, M. J. Bogan, M. Frank, J. Andreasson, B. Iwan, M. M. Seibert, J. Hajdu, A. Sakdinawat, J. Schulz, *et al.*, Phys. Rev. Lett. **104**, 064801 (2010).

[30] B. E. Warren, *X-ray diffraction* (Dover, 1990).

[31] V. Elser, *Noise limits in the assembly of diffraction data* (2007), URL `http://www.citebase.org/abstract?id=oai:arXiv.org:0709.3858`.

[32] R. A. Kirian, T. A. White, J. M. Holton, H. N. Chapman, P. Fromme, A. Barty, L. Lomb, A. Aquila, F. R. N. C. Maia, A. V. Martin, R. Fromme, *et al.*, Acta Cryst. A **67**, 131 (2011).

[33] N. D. Loh, M. J. Bogan, V. Elser, A. Barty, S. Boutet, S. Bajt, J. Hajdu, T. Ekeberg, F. R. N. C. Maia, J. Schulz, M. M. Seibert, B. Iwan, *et al.*, Phys. Rev. Lett. **104**, 225501 (2010).

[34] G. Bortel and M. Tegze, Acta Cryst. A **67**, 533 (2011).

[35] B. Moths and A. Ourmazd, Acta Cryst. A **67**, 481 (2011).

[36] R. Fung, V. Shneerson, D. K. Saldin, and A. Ourmazd, Nat. Phys. **5**, 64 (2008).

[37] G. Geloni, V. Kocharyan, and E. Saldin, J. Mod. Opt. **58**, 1391 (2011).

[38] W. Fawley, J. Frisch, Z. Huang, Y. Jiao, H.-D. Nuhn, C. Pellegrini, S. Reiche, and J. Wu, *Toward TW-level, hard X-ray pulses at LCLS*, LCLS TN-11-3, (2011).

[39] S.-K. Son, H. N. Chapman, and R. Santra, Phys. Rev. Lett. **107**, 218102 (2011).